

# Silicon-based all-optical photonic crystal neuromorphic synapses using $\text{Ge}_2\text{Sb}_2\text{Te}_5$

AMIR HOSSEIN ABDOLLAHI NOHOJI, PARVIZ KESHAVARZI, AND  
MOHAMMAD DANAIE\* 

*Faculty of Electrical and Computer Engineering, Semnan University, Semnan, Iran*

\*danaie@semnan.ac.ir

**Abstract:** This study investigates the design and implementation of all-optical synapse structures using photonic crystal configurations with a triangular lattice of circular holes to enhance efficiency and reduce the footprint of artificial synapses. The proposed structure uses phase change materials (PCM), especially  $\text{Ge}_2\text{Sb}_2\text{Te}_5$  (GST), to tune the transmitted wavelength precisely. Three-dimensional numerical simulations using the finite-difference time-domain (FDTD) and finite-element-method (FEM) indicate that these structures provide high-performance waveguide intersections with minimal cross-talk. Embedding two GST-PCM rods in this structure enables a high contrast in resonance wavelength transition between amorphous and fully crystalline states. By optimizing the radius of the GST-PCM rods, the highest contrast at the resonant transmission wavelength is achieved, allowing dynamic control of the transmission rate through changes in the crystallinity of the GST-PCM rods. The crystallinity is adjusted by varying the power and duration of laser radiation, demonstrating the high controllability of these structures. The proposed novel photonic crystal synapse structure combined with GST-PCM significantly reduces the energy consumption and dimensions of the optical synapse, which are crucial for developing artificial neural network devices, all-optical processors, and neuromorphic systems.

© 2025 Optica Publishing Group under the terms of the [Optica Open Access Publishing Agreement](#)

## 1. Introduction

In recent years, neuromorphic engineering [1–3] has emerged as an advanced and growing field of computer science and optical engineering. The aim of this field, inspired by the human brain, is to implement intelligent systems and process data using technologies such as artificial neurons [4]. Recent research in neuromorphic engineering has concentrated on creating artificial neural network models and synaptic structures [5] and has utilized various technologies to implement artificial synapses, including memristors [6], field effect transistors (FETs) [7,8], phase change memory [9–11], carbon nanotubes [12], and ferroelectric materials [13], and others [14–16].

Today, photonic neuromorphic structures have emerged in optical technologies, offering a new approach for simulating biological neuron functions and enhancing neuromorphic computing [17]. These structures use components, such as ring resonators [3,18–20], waveguides [21,22], and Mach-Zehnder interferometers [23], which enable them to perform computational tasks with higher speed and accuracy. Significant advances in optical and photonic technologies have led to numerous innovations in the design of neuromorphic synapses [24–26]. These innovations have enhanced the performance and efficiency of data processing systems, potentially increasing speed and reducing their physical size. These synapses are particularly ideal for high-speed and excellent-efficiency computing due to their high bandwidth and resistance to interference [14,27,28]. Smaller sizes of photonic devices, improved optical responses, and optimization of their structure can provide practical solutions for applications in optical integrated circuits (OICs).

Recent advances in photonic synapses have focused on the detailed investigation of various candidate materials [3,11,20,29,30], including metal oxides [31], perovskites [32], and nanoscale

materials [33]. In addition, phase change materials [11,28,34] have attracted the most attention in research efforts.

Photonic Mach-Zehnder memories using phase change materials have been proposed to simulate multilayer perceptron (MLP) neural networks [35,36]. In addition, in Ref. [11], a photonic synapse based on silicon waveguides and phase change materials (PCMs) is introduced, which allows the adjustment of synaptic weight through optical pulses. In Ref. [20] and Ref. [30], a synaptic network using PCM-based ring resonators is designed, which significantly improves the pattern recognition capabilities in neuromorphic systems.

Photonic synapses, which utilize the unique properties of phase change materials, can control the switching between crystalline and amorphous states. These materials can be triggered by the application of electric fields, temperature changes, or light irradiation. This capability enables researchers and engineers to precisely and control photonic synapses to perform diverse and complex processing operations in optical information-processing systems. These synapses can transmit light pulses of specific durations and energies to photonic structures containing phase change materials, allowing for the adjustment and optimization of synaptic weights. These capabilities enable the development of neuromorphic networks and support complex tasks such as pattern recognition and optical signal processing, advancing neuromorphic technologies and information-processing in areas like artificial neural network and image processing.

Recently, germanium-antimony-tellurium (GST) materials [21,37–41], with their unique properties, have been very effective and efficient as one of the basic PCMs for creating neuromorphic synapses [42]. The use of GST-PCMs, owing to their non-volatile nature opens up significant opportunities for photonic neuromorphic computing and enables data writing and erasing. This property enables researchers to modify the GST element across various crystal states [43] and establish synapses with precise, adjustable weights, enhancing the performance and efficiency of neuromorphic neural networks. The GST-PCMs are suitable for neuromorphic applications due to their unique properties, including significant differences in the real and imaginary parts of the refractive index between the amorphous and crystalline states, high repeatability, and fast switching speed [44]. These properties enable researchers to manipulate the state of these materials using various mechanisms such as electro-optical effects, thermal effects or light pulse irradiation, and use these materials to construct photonic switches or controllable synapses [45].

The development of phase-change synapse devices represents a significant advance in photonic neuromorphic computing. A pioneering approach in optical neuromorphic computing involves using photonic crystal-based optical synapses [28]. Photonic crystal (PhC) structures can be used as an alternative to traditional silicon photonic devices due to their unique optical properties and the ability to adjust the wavelength. These structures have precise control over optical frequencies and can limit the propagation of light waves in certain ranges and improve efficiency, size and power consumption in photonic integrated circuits (PIC) [46–48]. Photonic crystal technologies have advanced significantly through innovative research methods, primarily due to their capability to support compact and high-performance optical functionalities. These technologies are now utilized in both space-constrained environments and general-purpose optical systems [49]. These devices include various elements such as optical filters, sensors, amplifiers, all-optical memory cells, modulators, phase comparators, and switches, which are widely used in photonic crystal technology [50–54]. These elements play a crucial role in advanced technologies in this field by enabling the development of photonic devices with high performance, small dimensions, and compatibility with limited spaces [55,56].

In this paper, we focus on the design of an all-optical photonic crystal synapse structure. These structures offer advantages such as increased efficiency and reduced dimensions and technological complexity, which help to improve the performance and efficiency of optical-based artificial neural networks. The main goal of this research is to provide a new method to create a

synapse with high efficiency and minimal interference, increasing transmission and adapting to the requirements of neuromorphic systems. In this research, numerical 3D simulation using FEM and FDTD methods has been used. Previous studies have also confirmed the effectiveness of using optical synapses based on photonic structures in neuromorphic processing systems [24,28,57].

This research demonstrates that using photonic crystal structures as an efficient alternative to silicon-based photonic devices can lead to improved performance and efficiency of low dimension optical neural networks.

## 2. Perceptron neuron

Neurons are the main units of the central nervous system that receive, process and transmit information. Each neuron has essential components such as dendrite, nucleus, axon, and synapse (Fig. 1(a)). Dendrites are the branches that receive information from other neurons or peripheral stimuli and transmit it to the nucleus, where it is processed. When stimuli reach a certain threshold, the axon generates an action potential. Covered by a protective myelin layer, the axon conducts the electrical signal quickly to the synapses. Finally, this electrical signal is converted into a chemical signal at the synapses and transmitted to the next target neuron or cell. This process allows neurons to efficiently and quickly share information throughout the nervous system.

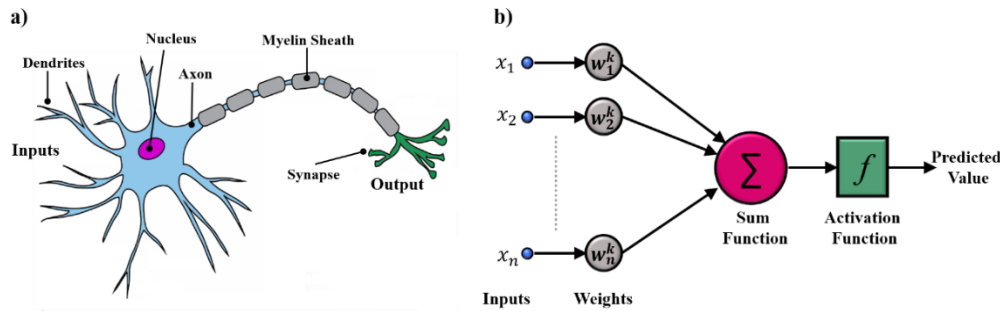


**Fig. 1.** Mechanism of a neuron. a) Biological neuron, the neuron receives information in the form of chemical signals from dendrites. When the sum of the inputs received through the dendrites is substantial enough to exceed the neuron's threshold, the nucleus generates an action potential. This action potential propagates along the axon with electrical changes. Upon reaching the synapses, the action potential causes the release of neurotransmitters in the synaptic space. b) A perceptron neuron. At each iteration step, blocks  $w_1$  to  $w_n$  weigh the input pulses, and then a summation block adds them together. An activation function compares the sum of the weighted inputs with a threshold value, which ultimately results in the generation of an output pulse in the neuron.

In an artificial perceptron neuron, incoming signals first pass through the neuron's synapses. Each of these synapses assigns a certain weight to the signals, which indicates their importance and influence in the neuron's decision-making process. After weighting, the signals are aggregated together. Then an activation function such as sigmoid function processes the aggregated signal. The activation function is critical in optical neuromorphic architectures because it allows neurons to model complex behaviors by converting input signals into nonlinear outputs. In the last step, the output of the activation function is compared with a threshold and the neuron produces an output signal.

This process (Fig. 1(b)) is essential in optical neural networks designed to simulate the behavior of biological neurons and optimize artificial neural computations.

In supervised learning algorithms, the network compares the output with the actual value and calculates the error rate. This error is usually measured using the mean squared error (MSE) function. Then, techniques such as the delta rule adjust and update the synaptic weights. This process involves the systematic modification of synaptic weights so that with each iteration, the algorithm gradually reduces the network error and increases the overall performance and accuracy of the neural network model.

Optimizing the weights through these algorithms lets the network to learn and produce more accurate outputs gradually. This supervised learning process is essential in artificial neural networks and optical neuromorphic systems, as it significantly increases the accuracy and efficiency of the network.

The relationships of a perceptron neuron can be summarized by the following equations:

- 1- A sum of weighted inputs:

$$z = \sum_{i=1}^n w_i^k x_i \quad (1)$$

where  $x_i$  is the inputs,  $w_i$  is the weight of synapses, and  $k$  is the number of epochs.

- 2- Activation function:

$$\text{Predicted value} = f(z) \quad (2)$$

where  $f$  is the activation function.

- 3- Error calculation:

$$E = \frac{1}{2}(\text{Predicted value} - \text{Actual value})^2 \quad (3)$$

- 4- Weight setting:

$$(w_i^k)_{\text{new}} = (w_i^k)_{\text{old}} - \eta \left( \frac{\partial E}{\partial w_i^k} \right)_{(w_i^k)_{\text{old}}} \quad (4)$$

where  $\eta$  is the learning rate.

These equations describe the basic operations of a perceptron neuron, including input accumulation, activation, error calculation, and weight adjustment.

### 3. Optical neuron mechanism

The operating speed of a silicon-based electronic perceptron neuron is limited by the electron transfer rate. Today, all-optical artificial neurons have made significant improvements in the performance speed of neuromorphic networks, so that these networks have found the ability to respond in a few nanoseconds. This advancement is attributable to the utilization of optical technologies such as optical waves for information transmission, which offer higher speeds compared to electronics. Optical technologies not only increase the speed of operations, but also facilitate parallel processing and greater efficiency in neural networks [57].

Although modern optical neuromorphic structures, such as ring resonators, waveguides, and Y-junctions utilizing phase change materials, have improved and operate faster than their electronic counterparts, they still have significant dimensions. This paper focuses on designing a synaptic structure using photonic crystal structures, which are significantly smaller than other optical neuromorphic structures.

As shown in Fig. 2, a continuous wave laser (CW-laser) generates the input optical signals and applies them to the synapses of the all-optical photonic crystal. All-optical photonic crystal synapses separate the wavelengths of each input signal that are tuned into the respective synapses using a photonic crystal cavity filter. Then, a multiplexer block sums the weighted signals

together. This process not only separates input signals based on wavelength but also adjusts the amplitude range of the signals using PCM. This capability aids in adjusting synaptic weights and facilitating communication between synapses.

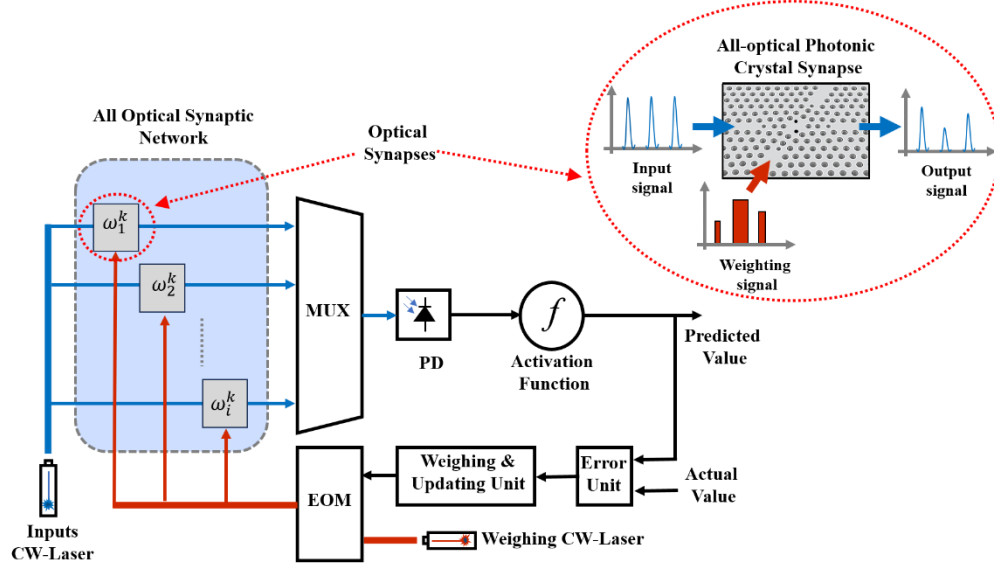


Fig. 2. Electro-optic action mechanism of an artificial neuron with an all-optical synapse.

In the next step of the process, a photodetector (PD) converts the optical signals processed by the photonic crystal synapses into electrical signals. The electrical signals are then fed to the activation function unit, which acts as a processor and calculates the output of the neuron. After the neuron's output is calculated, it is compared to the actual (or expected) value in error unit. Subsequently, a weighing and updating unit calculates the weight change rate for each synaptic connection separately. Then, the electro-optic modulator (EOM) unit generates the correction rate of each synaptic weight for the corresponding synapse. The output of this unit is applied to the target synapse via the red pathway (as shown in Fig. 2). In each cycle of the above steps, the synaptic weights are adjusted more accurately and the performance of the optical neural network is optimized.

Each photonic crystal synapse detects the wavelength associated with the updated weight signal using the cavity wavelength filtering capability. These synapses adjust their transmittance rates using embedded PCM rods. In Fig. 2, the blue path represents the passage of the input optical signal, while the red paths represent the update signals of the weight coefficients.

#### 4. Photonic crystal synapse

In this paper, we have proposed an all-optical synapse structure based on photonic crystals due to its much smaller dimensions compared to silicon-based structures. Previous studies [28] have used square lattice photonic crystal structures as optical synapses, which have faced challenges such as complexity in fabrication technology and high costs. Therefore, to address these issues, the use of silicon slab triangular lattice photonic crystal structures with air holes, as shown in Fig. 3, is proposed for improvement.

In comparison to the square photonic crystal structure that uses GaAs rods [28], the silicon-based triangular-lattice photonic crystal structure with air holes offers significant advantages. The use of silicon as the primary material not only simplifies the fabrication process but also reduces



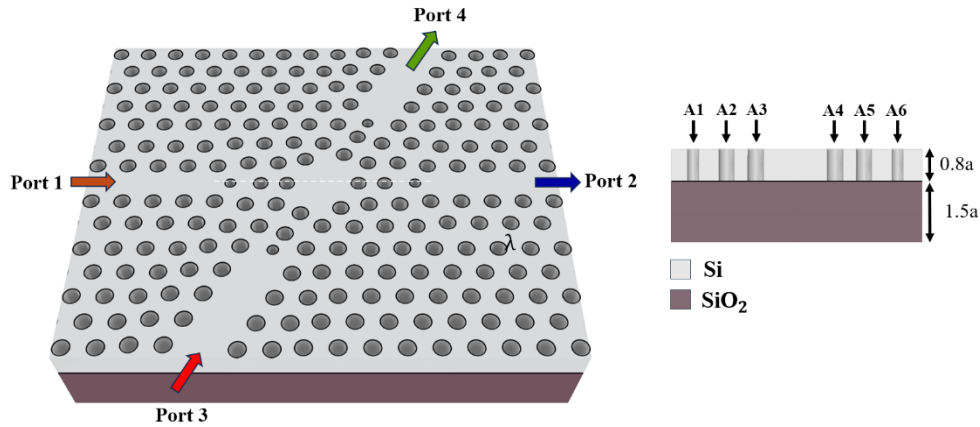


**Fig. 3.** Slab-hole type photonic crystal synapse. The proposed structure consists of silicon material on a  $\text{SiO}_2$  substrate, which creates a photonic crystal waveguide intersection structure by creating air holes. Holes A1 to A6 represent the radii of six critical holes located along the waveguide path from port 1 to port 2, and are responsible for tuning the transmission characteristics along this direction. The parameter “a” denotes the lattice constant of the photonic crystal.

production costs. Additionally, replacing GaAs rods with air holes enhances the mechanical stability of the structure, as air holes provide higher mechanical stability than GaAs rods. These changes contribute to improved performance and cost reduction in the design of optical synapses.

#### 4.1. Photonic crystal waveguide intersection

The proposed photonic crystal structure comprises circular air holes arranged in a triangular lattice within a silicon slab with a refractive index of 3.49, featuring a lattice constant of  $a = 0.424 \mu\text{m}$  and a thickness of  $0.8a$ . Each hole has a radius of  $r = 0.259a$ . By ignoring the two paths of the holes, horizontal and oblique waveguides (Fig. 4) are created in the proposed photonic crystal. These are crossed at their junction to form a cavity filter structure capable of tuning the pass wavelength resonance with minimal cross-talk.

In the proposed structure of Fig. 4, the radii of holes A2, A5, B2 and B5 are used to tune the transmission wavelength, while holes A1, A6, B1, and B6 are used as scattering holes that increase the transmission efficiency and reduce the full width at half maximum (FWHM). Holes A3, A4, B3, and B4 are also used to prevent cross-talk in waveguides.

In addition, to optimize the structure and reduce cross-talk, the position and radius of colored holes in Fig. 4 are optimized according to Table 1.

The transmission and cross-talk for the input states from ports 1 and 3 are shown in Fig. 5(a), (b), respectively. As can be seen, the passing wavelength in each path shows single-mode transmission, and more than 96% is transmitted from ports 1 to 2 at wavelength 1518 nm and 83% from ports 3 to 4 at wavelength 1594 nm. Also, the cross-talk is less than -25 dB and -51 dB respectively. The magnetic fields are shown in Fig. 5(a), (b) for the wavelength transmission modes from ports 1 to 2 and ports 3 to 4, respectively. As it is known, the intensity of the magnetic field in the cavity (intersection of waveguides) is maximum.

The FWHM and Q-factor [51] values are also obtained as 4.3 nm and 353 for the transfer from ports 1 to 2, respectively. To evaluate and validate the simulations, the signal transmission from ports 1 to 2 was simulated using FDTD and FEM methods and compared to coupled mode theory (CMT), showing good agreement (Fig. 6(a)).

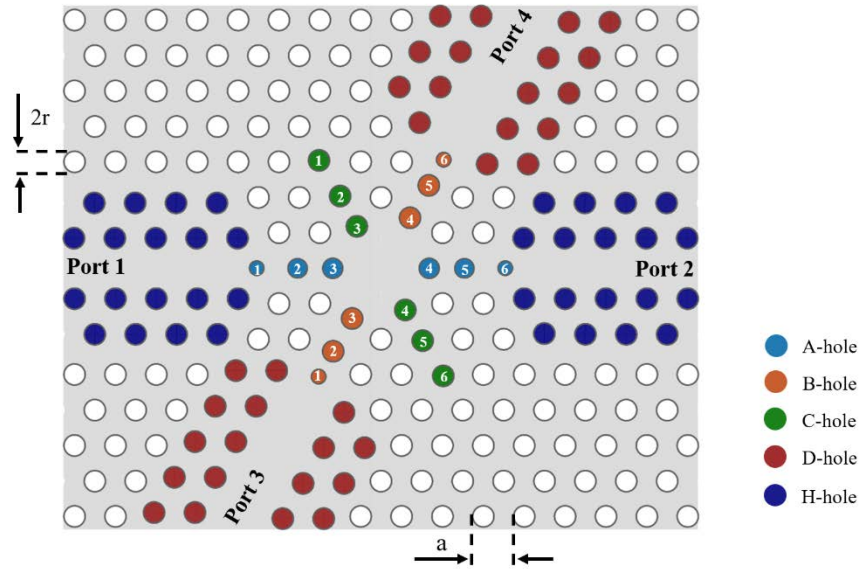


**Fig. 4.** Intersection of triangular lattice photonic crystal waveguides. A two-dimensional representation of the proposed structure is shown, which is created by ignoring the two paths of the holes, the photonic crystal waveguide intersection.

**Table 1. Optimized hole radius and displacement.**

Hole	Radius	Hole	Moving
A1, A6	0.177a	A1, A6, C1, C6	0.04a away from the center of the structure
A2, A5	0.235a	A2, A5, C2, C5	0.04a away from the center of the structure
A3, A4	0.245a	A3, A4, C3, C4	0.18a away from the center of the structure
B1, B6	0.177a	B1, B6	0.06a away from the center of the structure
B2~B5	0.259a	B2, B5	0.34a away from the center of the structure
C1~C6	0.259a	B3, B4	0.42a away from the center of the structure
D	0.259a	D	0.11a away from the center of the waveguide
H	0.259a	H	0.12a close to the center of the waveguide

In CMT, a structure is described based on the coupling between a cavity and waveguides, and the transfer function is provided using cavity quality factors ( $Q$ ) related to intrinsic loss ( $1/\tau_i$ ) and waveguide coupling loss ( $1/\tau_w$ ) and represented as  $Q_i = w_0\tau_i/2$  and  $Q_w = w_0\tau_w/2$ , respectively [58].  $W_0$  denotes the resonance frequency.

Since  $Q_w$  denotes the quality factor of total waveguide coupling losses, in this proposed structure,  $1/\tau_w$  represents the coupling loss of both waveguides on the cavity's sides ( $1/\tau_w = 1/\tau_{w_{in}} + 1/\tau_{w_{out}}$ ).

The cavity's transfer function can be expressed as Eq. (5).

$$tf = \frac{1/Q_w}{1/Q_w + 1/Q_i + 2j\lambda_n} \quad (5)$$

where  $\lambda_n = (\lambda_0 - \lambda)/\lambda$  represents the normalized wavelength and  $\lambda_0$  denotes the cavity resonance wavelength.

Also, the transmittance  $T$  from port 1 to 2 can be expressed as Eq. (6).

$$T = |tf|^2 \quad (6)$$

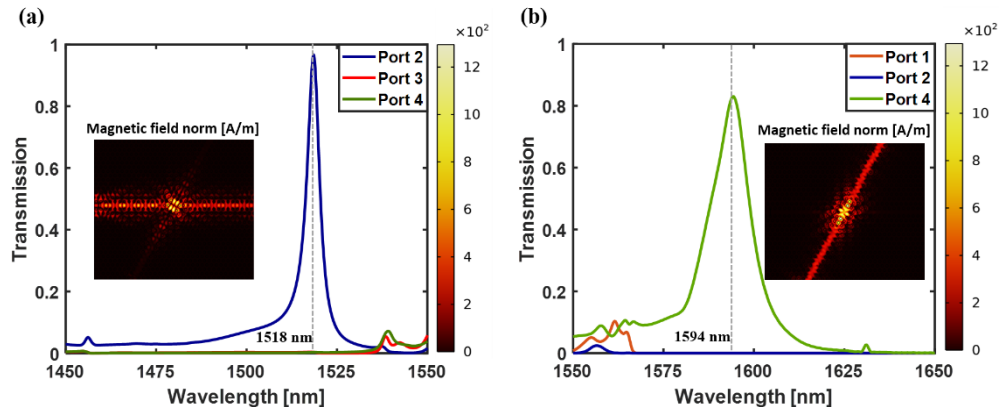


**Fig. 5.** (a) The magnetic field at the resonance wavelength and transmittance to port two and leakage at ports 3 and 4 when a Gaussian source with TE polarization is launched from port one, and (b) the magnetic field at the resonance wavelength and transmittance to port four and leakage at ports 1 and 2 when a Gaussian source with TE polarization is launched from port three.

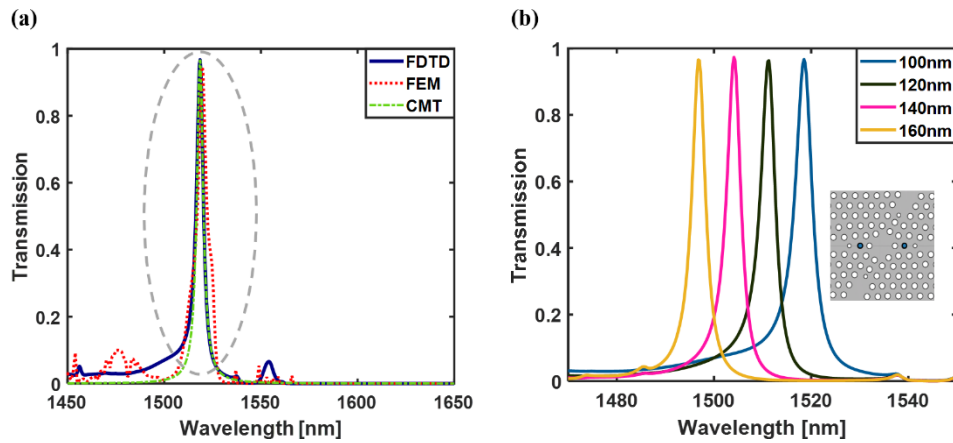


**Fig. 6.** (a) Comparison of photonic crystal waveguide intersection transmission using CMT, FDTD and FEM methods. (b) Transmission for different radii of holes A2 and A5 when input from ports 1 to 2 is applied. A 20 nm change in the radii of holes A2 and A5 results in a 7.2 nm change in resonant wavelength.

For the proposed structure,  $Q_i$  and  $Q_w$  were obtained as 23010 and 391, respectively.

Figure 6(b) shows the output transmission as a function of 20 nm variation in the radius of the A2 and A5 holes. These results show that the resonant wavelength of the cavity can be easily controlled and optimized by adjusting the radius of the A2 holes.

Fig. S1 shows the changes in the radius of holes A2, A5 and B2, B5, respectively, relative to the launch to ports 1 and 3.

Table 2 provides a comparative analysis of our proposed structure against previous designs, which shows that this structure has a smaller physical footprint and a significant reduction in insertion loss. This structure not only improves the performance of optical devices, but also has the potential to positively influence the development of advanced technologies in various fields, including optical communications, data processing, and neural networks.



**Table 2. The comparison of optical waveguide intersection structures.**

Year	Structure mechanism	Footprint [ $\mu\text{m}^2$ ]	Insertion Loss [dB]	Cross-talk [dB]	Ref.
2017	MDM	$21 \times 21$	0.46	-18	[59]
2017	cavity-like star	$5 \times 5$	0.75	-22.5	[60]
2018	PDM	$23 \times 23$	1.2	-25	[61]
2018	cavity	$4.8 \times 4.8$	0.6	-24	[62]
2019	MFE lens	$4.32 \times 4.32$	0.32	-15	[63]
2019	PDM	$6 \times 6$	0.2	-28	[64]
2020	intersection	$1.1 \times 1.1$	0.26	-40	[65]
2020	cosine tapers	$4.7 \times 4.7$	0.2	-35	[66]
2021	shaped-X	$2 \times 2.2$	0.2	-31	[67]
2022	multi-channel	$2 \times 2$	0.47	-84.8	[68]
2023	MMI	$13.6 \times 13.6$	0.76	-37.8	[69]
2023	SWG	$7.9 \times 5.9$	0.229	-35.6	[70]
2024	cavity	$2.97 \times 2.57$	0.17	-25	This work

#### 4.2. Photonic crystal synapse utilizing PCM rods

Figure 7(a) shows the Z-component of the magnetic field profile ( $H_z$ ) when a gaussian source with TE polarization is launched from port 1 and port 3. The maximum magnetic field is formed at the resonance wavelength within the cavity, exhibiting even symmetry in the diagonal waveguide path and odd quadrupole symmetry in the horizontal waveguide path.

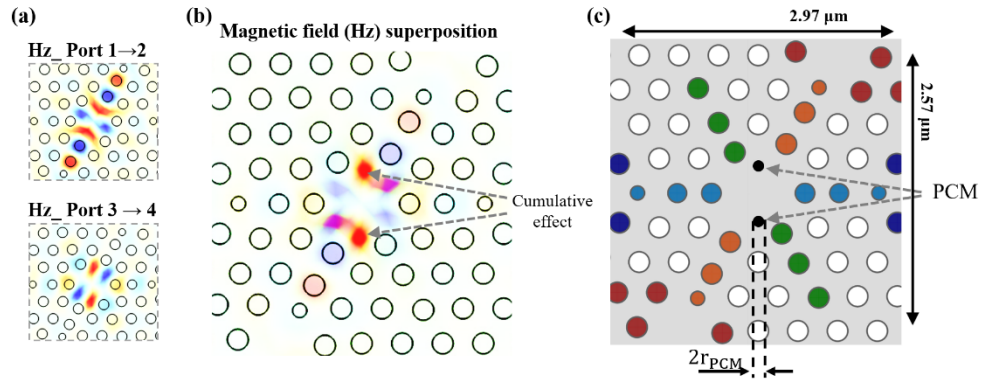


**Fig. 7.** (a) Z-component of the magnetic field ( $H_z$ ) during launches from ports 1 to 2 and from ports 3 to 4, (b) superposition of the Z-component of the magnetic field ( $H_z$ ), (c) photonic crystal synapse utilizing PCM rods. The Z-component of the magnetic field shows a significant increase at two points (marked in dark red) when the signal is transmitted through both the horizontal and diagonal waveguide paths.

It can be seen that the intensity of the magnetic field is maximum at the two common points of the structure, where the cumulative effect of the  $H_z$ -field is the highest. These common points have the greatest impact on the transfer from ports 1 to 2 and from ports 3 to 4.

The combination of the Z-components of the magnetic fields ( $H_z$ ) when launched from ports 1 and 3 results in a significant increase and intensification of the magnetic field at two specific points (Fig. 7(b)). This process leads to overlapping and interference of magnetic fields at these points, which leads to a significant increase in field intensity. By placing the PCM at the common points of the magnetic fields, the percentage transmission of the resonant wavelength in both waveguide paths can be precisely controlled. Figure 7(c) shows the proposed structure equipped with PCM. In the proposed approach, GST ( $\text{Ge}_2\text{Sb}_2\text{Te}_5$ ) and GSST ( $\text{Ge}_2\text{Sb}_2\text{Se}_4\text{Te}_1$ ) materials have been used as PCM. These materials enable dynamic tuning of optical properties and facilitate greater flexibility and efficiency in optical signal processing applications. Fig. S2 shows the graph of the real and imaginary parts of the refractive index for the GST and GSST materials [20,35].

In the crystallization process of phase-change materials such as  $\text{Ge}_2\text{Sb}_2\text{Te}_5$ , the crystallization temperature ( $T_c$ ) is the primary factor in initiating the transition from the amorphous to the crystalline state. Specifically, for GST-PCM, the onset of crystallization, characterized by the nucleation and subsequent growth of the crystalline lattice, occurs within a defined temperature range of 413–423 °K [71,72].

In GST materials, when the temperature is increased to more than the crystallization temperature ( $\sim T_c > 420$  °K) by applying long-duration light pulses, the material gradually transforms into a crystalline state [73]. This phase change leads to a change in the refractive index and optical properties the PCM material. Furthermore, at temperatures above the melting point ( $T_m = 873$  °K), applying a short, high-power pulse followed by rapid cooling to prevent re-crystallization can return the material to the amorphous state [74–76]. These properties introduce GST as a non-volatile and temperature-sensitive material that can rapidly control the transmission of optical signals by applying specific light pulses. Fig. S3 shows the phase diagram and transition process between crystalline and amorphous states in GST materials [77].

The use of PCM materials in this structure changes the optical properties and light transmission characteristics by changing the phase and refractive index of the PCM material in response to temperature changes. This feature can lead to the control and optimization of resonant wavelength transmission in these systems, which is very important in photonic and optical technologies.

Fig. S4 shows the transmission from ports 1 to 2 under the conditions of amorphous and fully crystalline states for the radius variation of GST and GSST rods. The greatest contrast in resonant wavelength transmission between the amorphous and fully crystalline states occurs with an optimal rod radius of 85.5% for GST and 92.4% for GSST materials at rod radii of 61.9 nm and 83.3 nm, respectively. The structure transmission modulation factor for GST and GSST materials is shown using the figure of merit function (FOM) (Eq. (7)), which is 97.5% and 98% for GST and GSST, respectively.

$$FOM \% = \frac{T_{r_{amorphous}} - T_{r_{crystal}}}{T_{r_{amorphous}} + T_{r_{crystal}}} \times 100 \quad (7)$$

where  $T_r$  is transmission.

In this approach, although the FOM value for GSST is higher than that of GST materials, we have used GST materials for phase change materials due to the non-availability of specific thermal equations for GSST.

The effective permittivity of GST is described based on the changes in the crystallization coefficient of GST ( $0 < \beta < 1$ ) based on the Lorentz–Lorenz equation in Eq. (8) [78]. In addition, the changes in the crystallization coefficient of GST due to temperature ( $T$ ) changes are also calculated using Eq. (9) and Eq. (10) [74,79]. Therefore, by applying temperature to GST, both the real ( $n$ ) and imaginary ( $k$ ) parts of the refractive index of GST can be changed according to Eq. (11).

$$\varepsilon_{eff_{GST}}(\beta) = \frac{\varepsilon_a(\varepsilon_c + 2) + 2\beta(\varepsilon_c - \varepsilon_a)}{\varepsilon_c + 2 - \beta(\varepsilon_c - \varepsilon_a)} \quad (8)$$

where  $\varepsilon_a$  and  $\varepsilon_c$  are amorphous and crystallization permittivity of GST, respectively.

$$\beta(T_{\text{kelvin}}) = \frac{e^A}{1 + e^A} \quad (9)$$

$$A = \frac{T_{\text{kelvin}} - 615}{30} \quad (10)$$

$$\sqrt{\varepsilon_{\text{effGST}}(\beta)} = n + ik \quad (11)$$

One of the methods used to increase the temperature of GST materials is using laser beams with predetermined parameters of power and duration. This approach is a practical tool to modify the thermal and optical properties of GST materials. By fine-tuning the power and duration of the laser applied to the GST material, the heating of the GST can be precisely controlled.

The laser intensity at the GST material's depth can be calculated using the Beer-Lambert law [80], as shown in Eq. (12).

$$I_{d_{\text{GST}}} = (1 - R)I_0 e^{-\alpha d_{\text{GST}}} \quad (12)$$

where  $I_0$  represents the incident laser intensity,  $\alpha$  is the material's absorption coefficient, and  $d_{\text{GST}}$  is the depth within the GST.  $R$  denotes the reflectivity of the incident laser.

The temperature of the GST rods is calculated from the heat transfer equation [81,82] (Eq. (13)), which incorporates laser power and duration.

$$\rho c_p \frac{\partial T}{\partial t} + \rho c_p U \cdot \nabla T = \nabla \cdot (k \nabla T) + Q_{rh} \quad (13)$$

Here,  $Q_{rh}$  is considered resistive loss in the GST rods, which can be derived from Eqs. (14-16).  $c_p$  and  $\rho$  represent the specific heat capacity at constant pressure and the density of the material, respectively.

$$Q_{rh} = \frac{1}{2} \text{Re}(J \cdot E^*) \quad (14)$$

$$E = \sqrt{\frac{2I_{d_{\text{GST}}}}{C\varepsilon_0 n}} \quad (15)$$

$$J = 2nk\omega\varepsilon_0 E \quad (16)$$

where  $J$  is electric current density,  $E$  is electric field,  $C$  is the speed of light in a vacuum,  $\varepsilon_0$  is permittivity of free space, and  $n$  and  $k$  represent the real and imaginary parts of the refractive index of GST-PCM, respectively.

## 5. Discussion and comparisons

Figure 8(a) shows the transmission characteristics from ports 1 to 2 in terms of changes in the crystallinity of the GST rods. By adjusting the GST crystallinity factor between 0 and 1, the light transmission can be controlled between 0.01 and 0.86. In the proposed approach, the crystallinity coefficient of the GST rods can be changed by using laser radiation with specific power and duration from ports 3 to 4. Therefore, the transfer rate from ports 1 to 2 can be controlled accordingly. Figure 8(b) shows the degree of crystallization of GST materials under different crystallization coefficients using laser irradiation with  $100 \text{ mW}/\mu\text{m}^2$  from port 3. The graph shows that adjusting the coefficient from 0-1 requires a laser irradiation time in the range of 0.2-0.9 ns. These findings emphasize the potential of laser irradiation as a precisely controlled tool for crystallization changes of GST materials, making it highly applicable in optical synapses and neuromorphic systems.

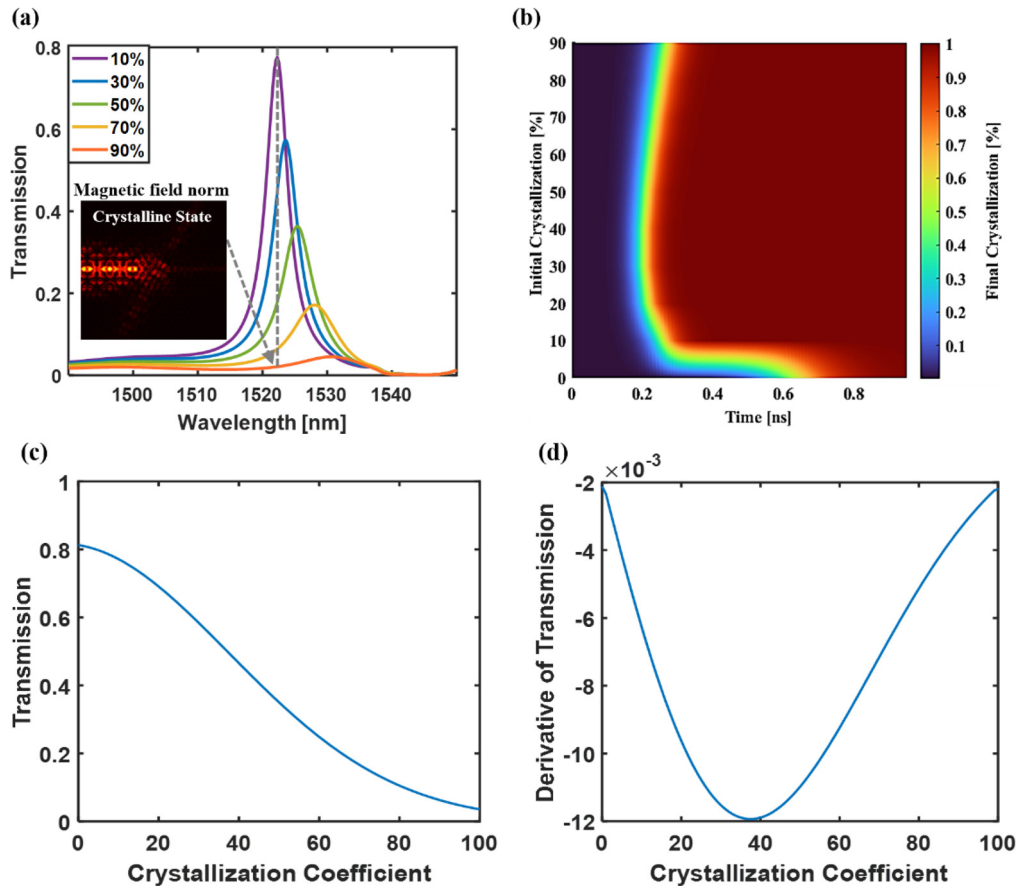


**Fig. 8.** (a) Transmission of photonic crystal synapses for different crystallization coefficients. (b) The crystallization degree of GST rods at different initial coefficients using  $100 \text{ mW}/\mu\text{m}^2$  laser irradiation from port 3. Complete crystallization of GST rods takes between 0.2-0.9 ns, with the longest time observed in the fully amorphous state. (c) Transmission as a function of the GST crystallization coefficient. (d) Derivative of optical transmission with respect to the crystallization coefficient

To evaluate the sensitivity of the proposed structure to variations in the crystallization coefficient of GST, the optical transmission as a function of crystallization level (Fig. 8(c)) and its derivative (Fig. 8(d)) were analysed. The results indicate that the transmission response changes non-linearly with  $\beta$ , with maximum sensitivity observed in the intermediate region of the curve.

Figure 9(a) shows the change of the crystallization coefficient in GST material in response to changes in time and laser power applied from ports 3 to 4. It shows that increasing the laser power reduces the time required to change the crystallization coefficient of GST materials. In other words, higher laser power enables the crystallinity coefficient of GST material to be adjusted from 0-100% in less time. Figure 9(b) shows the change of the crystallization coefficient in GST-PCM rods under laser irradiation with a power density of  $100 \text{ mW}/\mu\text{m}^2$ . As shown in Fig. 9(b), laser irradiation from 0-0.3 ns does not have much effect on the crystallinity change of GST-PCM rods. Although the laser irradiation causes heating of the GST-PCM rods (the temperature profile is also shown in Fig. 9(b)), the temperature of the GST-PCM rods remains below the crystallization temperature of GST. After 0.3 ns of laser irradiation, the GST temperature reaches the desired level to start the crystallization process, and the crystallization coefficient increases as described

in Eq. (9). This process continues for 0.9 ns until the GST-PCM rods are fully crystallized. Also, as shown in Fig. 9(a), with increasing laser power density, the time required for the crystallization process decreases.

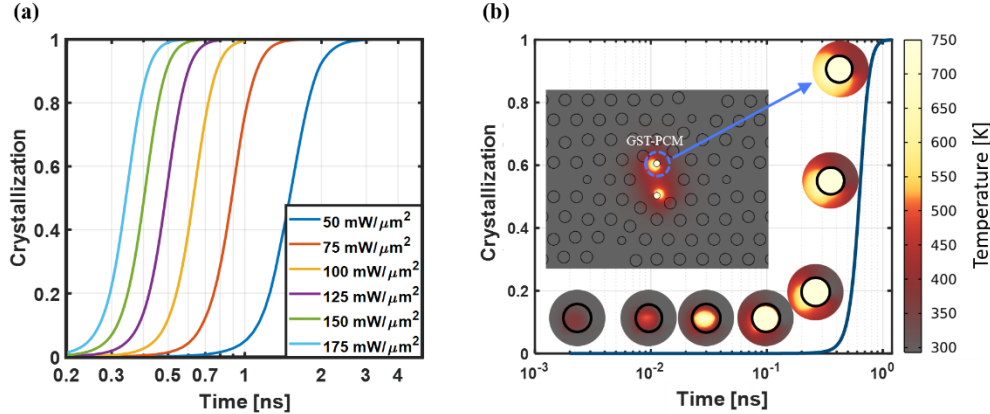


**Fig. 9.** (a) The effect of laser power density applied from port three on the crystallization rate of GST materials. The time required for the crystallization of GST rods decreases with the increase of the applied laser power density. Specifically, at a power density of 175 mW/μm², the time of the crystallization process varies between 0.2-0.8 ns. (b) Thermal profile and crystallization process of GST rods as a function of time with a 100 mW/μm² laser launched from port 3. Laser irradiation up to 0.3 ns has less effect on the crystallization of GST-PCM rods. Although the GST temperature increases, it remains below the crystallization temperature. After 0.3 ns, the temperature reaches the crystallization point and the rods gradually crystallize.

It is important to note that the time reported in Figs. 8 and 9 refers to the duration of the laser pulse applied with a specified power to raise the temperature of the GST region to the crystallization temperature, not the complete crystallization process, which involves nucleation and crystal growth.

Previous experimental studies [83,84] have demonstrated that the complete crystallization time in GST layers typically occurs within tens of nanoseconds, a duration that is significantly influenced by the material's structure, dimensions, and the surrounding environment. These investigations have provided insights into the entire crystallization mechanism, from the onset of nucleation to the evolution of the crystalline structure, a phenomenon governed by the thermal kinetics of the material.

The significant reduction in thermal mass at these scales results in a faster temperature rise in the material, thereby reducing the time required to reach the crystallization threshold temperature. Given the inverse relationship between heating rate and thermal mass, the use of phase-changing elements at the nanoscale enables the material to reach the necessary temperature for crystallization initiation with short laser pulses. Consequently, while the desired temperature is achieved within sub-nanosecond timescales, the full crystallization process, as reported in earlier studies, occurs over tens of nanoseconds.

Furthermore, based on the above considerations, in this study, the crystallization behaviour of GST under the influence of rapid and high-power laser pulses has been modelled using a temperature-dependent logistic function, as described by Eqs. (5) and (6). In contrast to conventional time-dependent models such as the Johnson-Mehl-Avrami-Kolmogorov (JMAK) equation [85,86], which analyse the kinetics of crystallization as a function of time, nucleation rate, and crystal growth dimensionality, the model employed in this work focuses solely on the



relationship between temperature and the estimated crystallization fraction at the end of the heating phase.

In other words, this model estimates the extent to which the material crystallizes—relative to a fully crystalline state—after the local temperature reaches a certain value, without analysing the complete temporal evolution of the crystallization process, including growth and nucleation.

This approach is fully aligned with the primary objective of the present study, which is to investigate the thermal stability and the resulting crystallization fraction of GST under rapid, localized heating induced by an optical pulse. Within this framework, the laser pulse duration (as shown in Fig. 9) is interpreted merely as the time required for the GST region to reach the target temperature necessary to initiate crystallization, and not the total time needed to complete the entire crystallization process. In contrast, the JMAK model can be employed in future studies to further analyse the time-dependent dynamics of crystal growth after the material has reached the critical temperature.

Additionally, the proposed structure utilizes GST regions with extremely small volumes, which, due to their low thermal mass, experience significantly faster heating in response to laser pulses. This property enables the material to reach the crystallization threshold within an extremely short timescale.

In summary, the presented model describes the stable crystallization fraction of GST under laser-induced thermal conditions and does not account for the kinetic aspects of the crystallization process over time, as addressed in kinetic models such as JMAK. Nonetheless, the development of hybrid temperature- and time-dependent models for a more comprehensive analysis of crystallization dynamics can be considered in future studies.

Table 3 compares the synaptic and optoelectronic structures found in previous research and shows that our proposed structure is significantly smaller. A structure with smaller dimensions leads to occupying less space, which in turn increases the density in optical integrated circuits. Considering the importance of increasing the density of neuromorphic synapses in optical neural networks, our design optimally integrates these neuromorphic synapses using photonic crystals in photonic integrated circuits. Ultimately, the use of such structures can provide innovative solutions to our computational challenges and pave the way for further advances in the field of neuromorphic computing. The energy consumption in Table 3 is calculated using Eq. (17) [87].

$$\text{Energy} = I_0 \times S \times t \quad (17)$$

where  $S$ ,  $I_0$ , and  $t$  are the area of the structure under laser irradiation, the power density, and the duration of laser irradiation for weight adjustment, respectively.

To assess the fabrication tolerance of the proposed structure, a comprehensive analysis was carried out by examining the sensitivity of its optical performance to deviations in critical geometric parameters. Specifically, variations in the radii of the A, B, and C type holes were analysed, and the results, depicted in Fig. S5, confirm that the optical behaviour remains stable under moderate dimensional fluctuations.

Furthermore, the influence of changes in the GST rods radii on the transmission response is analysed in Fig. S4, while the corresponding wavelength shift is presented in Fig. S6. To provide a consolidated overview, Table 4 summarizes the sensitivity of key optical metrics to various geometric deviations. These results demonstrate that the proposed structure maintains reliable performance within standard fabrication tolerances, highlighting its suitability for implementation in dense photonic neural networks and its compatibility with large-scale photonic integration.

## 6. Conclusion

In this article, we have investigated the design and implementation of all-optical synapses using photonic crystal structure in order to increase the efficiency and reduce the dimensions of artificial synapses. The proposed structure uses phase change materials, specifically GST-PCM,

**Table 3. Comparison of previous studies on artificial synaptic structures.**

Year	Device structure	Active material	Footprint [ $\mu\text{m}^2$ ]	Energy consumption	Reference
2016	Bottom gate	IGZO/ $\text{Al}_2\text{O}_3$	$20 \times 40$	$\sim 13$ pJ	[88]
2017	Two terminals	IGZO, ISZO, ISO, IZO	$180 \times 70$	-	[89]
2017	Tapered waveguide	$\text{Ge}_2\text{Sb}_2\text{Te}_5$	$36 \times 14$	$\sim 404$ pJ	[11]
2017	Crossing waveguide	$\text{Ge}_2\text{Sb}_2\text{Te}_5$	$30 \times 30$	-	[41]
2017	Bottom gate	Graphene/SWNTs	$30 \times 90$	$\sim 6$ nJ	[90]
2018	Micro ring resonator	$\text{Ge}_2\text{Sb}_2\text{Te}_5$	$72 \times 55$	$\sim 620$ pJ	[43]
2018	Two-terminal	SiNCs	$2000 \times 2000$	$\sim 4$ pJ	[91]
2018	Bottom gate	GZO/chitosan	$80 \times 1000$	-	[92]
2019	Bottom gate	IZO	$30 \times 100$	$\sim 35$ nJ	[93]
2019	Waveguide	$\text{Ge}_2\text{Sb}_2\text{Te}_5$	$1530 \times 120$	$\sim 710$ pJ	[20]
2019	lateral gate	$\text{In}_2\text{O}_3$	$80 \times 1600$	$\sim 40$ nJ	[94]
2019	Micro ring resonator	$\text{Ge}_2\text{Sb}_2\text{Se}_4\text{Te}_1$	$590 \times 380$	$\sim 5.5$ $\mu\text{J}$	[95]
2019	Bottom gate	ITO/chitosan	$80 \times 1000$	$\sim 3.9$ $\mu\text{J}$	[96]
2022	Micro ring resonator	$\text{In}_2\text{Se}_3$	$25 \times 17$	$\sim 250$ pJ	[97]
2023	Multi-mode interference	$\text{Ge}_2\text{Sb}_2\text{Te}_5$	$115 \times 66$	-	[98]
2024	Square rod waveguide intersection	$\text{Ge}_2\text{Sb}_2\text{Te}_5$	$5.4 \times 5.4$	-	[28]
2024	Slab triangular waveguide intersection	$\text{Ge}_2\text{Sb}_2\text{Te}_5$	$2.97 \times 2.57$	$\sim 267$ pJ	This work

**Table 4. Transmission and Wavelength Sensitivity to Radius Changes.**

Excitation Direction	Varied Element ( $\pm 5$ nm)	Wavelength Shift %	Transmission Drift ( $\Delta T$ )
Port 1 to 2	A3	0.62	0.011
	B3	0.28	0.003
	C3	0.41	0.006
	C2	0.19	0.004
	GST-am	0.17	0.119
	GST-cry	0.15	0.055
Port 3 to 4	A3	0.29	0.009
	B3	0.41	0.125
	C3	0.25	0.010
	C2	0.05	0.000
	GST-am	0.13	0.014
	GST-cry	0.29	0.212

to precisely tune the transmitted wavelength. The simulation results show that the slab-hole type photonic crystal structure with lattice constant  $a = 0.424 \mu\text{m}$  and cavity radius  $0.259a$  can create a low cross-talk intersection waveguide by ignoring the two paths of the holes. The proposed structure can transmit an optical signal through a horizontal waveguide with 96% efficiency and -25 dB cross-talk. In addition, we calculated the FWHM and Q-factor of the proposed structure as 4.3 nm and 353, respectively, which indicates the high efficiency of the structures in single-mode signal transmission. By adding two GST-PCM rods to the structure, we created a high contrast in resonant wavelength transition between the amorphous and fully crystalline states of the PCM rods. The maximum contrast at the resonant wavelength was obtained with an optimal GST-PCM rods radius of 61.9 nm. Laser irradiation with a power density of  $100 \text{ mW}/\mu\text{m}^2$  showed that the crystallization time of GST rods can vary from 0.2 to 0.9 ns, which shows the ability to adjust the dynamics of the proposed structure. Furthermore, the findings show that changes in the crystallinity of the GST rods can control the transmission from 1–86%. Adjusting the time and power of the applied laser radiation changes the crystallinity of the GST rods, which shows the high controllability of the structure. Hole-type photonic crystal structures are generally more optimized with respect to fabrication cost and process complexity compared to rod-type photonic crystal structures. Their distinctive geometric configuration reduces the need for complex fabrication processes, making them highly suitable for large-scale integration and widespread application in next-generation all-optical neuromorphic processors and optical artificial synapses. This study showed that the use of photonic crystal structures and phase change materials can lead to improved processing speed and reduced dimensions in optical synapse systems, which is very critical in the design of all-optical neuromorphic systems. Photonic crystal structures, by reducing dimensions and increasing efficiency, significantly facilitate further research and development of advanced technologies in optical processors and optical artificial neuromorphic systems.

**Disclosures.** The authors declare no conflict of interests. The authors also have no relevant financial or non-financial interests to disclose.

**Data availability.** Data underlying the results presented in this paper are not publicly available at this time but may be obtained from the authors upon reasonable request.

**Supplemental document.** See [Supplement 1](#) for supporting content.

## References

1. J.-Q. Yang, R. Wang, Y. Ren, *et al.*, “Neuromorphic engineering: from biological to spike-based hardware nervous systems,” *Adv. Mater.* **32**(52), 2003610 (2020).
2. C. Mead, “How we created neuromorphic engineering,” *Nat. Electron.* **3**(7), 434–435 (2020).
3. I. Chakraborty, G. Saha, and K. Roy, “Photonic in-memory computing primitive for spiking neural networks using phase-change materials,” *Phys. Rev. Appl.* **11**(1), 014063 (2019).
4. S. Chen, T. Zhang, S. Tappertzhofen, *et al.*, “Electrochemical-memristor-based artificial neurons and synapses—fundamentals, applications, and challenges,” *Adv. Mater.* **35**(37), 2301924 (2023).
5. B. Sun, T. Guo, G. Zhou, *et al.*, “Synaptic devices based neuromorphic computing applications in artificial intelligence,” *Mater. Today Phys.* **18**, 100393 (2021).
6. S. Kumar, X. Wang, J. P. Strachan, *et al.*, “Dynamical memristors for higher-complexity neuromorphic computing,” *Nat. Rev. Mater.* **7**(7), 575–591 (2022).
7. X. Li, Y. Liu, J. Zhang, *et al.*, “Flexible artificial synapses based on field effect transistors: from materials, mechanics towards applications,” *Adv. Intell. Syst.* **4**(9), 2200015 (2022).
8. G. Zhong, M. Zi, C. Ren, *et al.*, “Flexible electronic synapse enabled by ferroelectric field effect transistor for robust neuromorphic computing,” *Appl. Phys. Lett.* **117**(9), 092903 (2020).
9. W. Zhou, N. Farmakidis, X. Li, *et al.*, “Artificial biphasic synapses based on nonvolatile phase-change photonic memory cells,” *Phys. Status Solidi RRL* **16**(9), 2100487 (2022).
10. S. R. Nandakumar, I. Boybat, M. L. Gallo, *et al.*, “Experimental demonstration of supervised learning in spiking neural networks with phase-change memory synapses,” *Sci. Rep.* **10**(1), 8080 (2020).
11. Z. Cheng, C. Ríos, W. H. P. Pernice, *et al.*, “On-chip photonic synapse,” *Sci. Adv.* **3**(9), e1700160 (2017).
12. F. Xia, T. Xia, L. Xiang, *et al.*, “Carbon nanotube-based flexible ferroelectric synaptic transistors for neuromorphic computing,” *ACS Appl. Mater. Interfaces* **14**(26), 30124–30132 (2022).

13. B. Tian, L. Liu, M. Yan, *et al.*, “A robust artificial synapse based on organic ferroelectric polymer,” *Adv. Electron. Mater.* **5**(1), 1800600 (2019).
14. J. Zhang, S. Dai, Y. Zhao, *et al.*, “Recent progress in photonic synapses for neuromorphic systems,” *Adv. Intell. Syst.* **2**(3), 1900136 (2020).
15. Z. Wang, S. Joshi, S. E. Savel’ev, *et al.*, “Memristors with diffusive dynamics as synaptic emulators for neuromorphic computing,” *Nat. Mater.* **16**(1), 101–108 (2017).
16. S. Tir, M. Shalchian, and M. Moezzi, “Design of bioinspired tripartite synapse analog integrated circuit in 65-nm CMOS Technology,” *J. Comput. Electron.* **19**(3), 1313–1328 (2020).
17. C. Zhu, H. Liu, W. Wang, *et al.*, “Optical synaptic devices with ultra-low power consumption for neuromorphic computing,” *Light: Sci. Appl.* **11**(1), 337 (2022).
18. F. D.-L. Coarer, “Neuromorphic computing using nonlinear ring resonators on a silicon photonic chip,” Centrale-Supélec (2020).
19. S. S. Sharif, H. Karimkhani, and Y. M. Banad, “Exploring nonlinear activation function within microring resonators for all-photonic neuromorphic computing,” in *Physics and Simulation of Optoelectronic Devices XXXII* (2024), Vol. 12880, pp. 189–193.
20. J. Feldmann, N. Youngblood, C. D. Wright, *et al.*, “All-optical spiking neurosynaptic networks with self-learning capabilities,” *Nature* **569**(7755), 208–214 (2019).
21. F. Brücknerhoff-Plückelmann, J. Feldmann, C. D. Wright, *et al.*, “Chalcogenide phase-change devices for neuromorphic photonic computing,” *J. Appl. Phys.* **129**(15), 151103 (2021).
22. J. T. Kim, J. Song, and C. S. Ah, “Optically readable waveguide-integrated electrochromic artificial synaptic device for photonic neuromorphic systems,” *ACS Appl. Electron. Mater.* **2**(7), 2057–2063 (2020).
23. Y. Zhang, H. Deng, E. Soltanian, *et al.*, “A nonlinear activation function for optical neural networks using a Mach-Zehnder interferometer with a III-V-on-Si amplifier,” in *The European Conference on Lasers and Electro-Optics* (2023), p. ck\_13\_2.
24. L. De Marinis, M. Cococcioni, P. Castoldi, *et al.*, “Photonic neural networks: a survey,” *IEEE Access* **7**, 175827–175841 (2019).
25. B. Xu, Y. Huang, Y. Fang, *et al.*, “Recent progress of neuromorphic computing based on silicon photonics: Electronic-photonic Co-design, device, and architecture,” *Photonics* **9**(10), 698 (2022).
26. R. V. Kutluyarov, A. G. Zakoyan, G. S. Voronkov, *et al.*, “Neuromorphic photonics circuits: contemporary review,” *Nanomaterials* **13**(24), 3139 (2023).
27. Y.-X. Hou, Y. Li, Z.-C. Zhang, *et al.*, “Large-scale and flexible optical synapses for neuromorphic computing and integrated visible information sensing memory processing,” *ACS Nano* **15**(1), 1497–1508 (2021).
28. A. H. A. Nohji, P. Keshavarzi, and M. Danaie, “A photonic crystal waveguide intersection using phase change material for optical neuromorphic synapses,” *Opt. Mater.* **151**, 115372 (2024).
29. X. Guo, J. Xiang, Y. Zhang, *et al.*, “Integrated neuromorphic photonics: synapses, neurons, and neural networks,” *Adv. Photonics Res.* **2**(6), 2000212 (2021).
30. I. Chakraborty, G. Saha, A. Sengupta, *et al.*, “Toward fast neural computing using all-photonic phase change spiking neurons,” *Sci. Rep.* **8**(1), 12980 (2018).
31. J. Wang, Y. Li, Y. Yang, *et al.*, “Top-gate electric-double-layer IZO-based synaptic transistors for neuron networks,” *IEEE Electron Device Lett.* **38**(5), 588–591 (2017).
32. L. Qian, Y. Sun, M. Wu, *et al.*, “A lead-free two-dimensional perovskite for a high-performance flexible photoconductor and a light-stimulated synaptic device,” *Nanoscale* **10**(15), 6837–6843 (2018).
33. L. Shao, H. Wang, Y. Yang, *et al.*, “Optoelectronic properties of printed photogating carbon nanotube thin film transistors and their application for light-stimulated neuromorphic devices,” *ACS Appl. Mater. Interfaces* **11**(12), 12161–12169 (2019).
34. Z. Gong, F. Yang, L. Wang, *et al.*, “Phase change materials in photonic devices,” *J. Appl. Phys.* **129**(3), 030902 (2021).
35. M. Miscuglio, J. Meng, O. Yesiliurt, *et al.*, “Artificial synapse with mnemonic functionality using GSST-based photonic integrated memory,” in *2020 International Applied Computational Electromagnetics Society Symposium (ACES)* (2020), pp. 1–3.
36. I. A. D. Williamson, T. W. Hughes, M. Minkov, *et al.*, “Reprogrammable electro-optic nonlinear activation functions for optical neural networks,” *IEEE J. Sel. Top. Quantum Electron.* **26**(1), 1–12 (2020).
37. N. Youngblood, C. Ríos, E. Gemo, *et al.*, “Tunable volatility of Ge<sub>2</sub>Sb<sub>2</sub>Te<sub>5</sub> in integrated photonics,” *Adv. Funct. Mater.* **29**(11), 1807571 (2019).
38. S. G.-C. Carrillo, A. Lugnan, E. Gemo, *et al.*, “System-level simulation for integrated phase-change photonics,” *J. Lightwave Technol.* **39**(20), 6392–6402 (2021).
39. T. Ferreira De Lima, A. N. Tait, A. Mehrabian, *et al.*, “Primer on silicon neuromorphic photonic processors: architecture and compiler,” *Nanophotonics* **9**(13), 4055–4073 (2020).
40. B. J. Shastri, A. N. Tait, T. de Lima, *et al.*, “Photonics for artificial intelligence and neuromorphic computing,” *Nat. Photonics* **15**(2), 102–114 (2021).
41. J. Feldmann, M. Stegmaier, N. Gruhler, *et al.*, “Calculating with light using a chip-scale all-optical abacus,” *Nat. Commun.* **8**(1), 1256 (2017).

42. M. Xu, X. Mai, J. Lin, *et al.*, "Recent advances on neuromorphic devices based on chalcogenide phase-change materials," *Adv. Funct. Mater.* **30**(50), 2003419 (2020).
43. J. Zheng, A. Khanolkar, P. Xu, *et al.*, "GST-on-silicon hybrid nanophotonic integrated circuits: a non-volatile quasi-continuously reprogrammable platform," *Opt. Mater. Express* **8**(6), 1551–1561 (2018).
44. T. Cao, L. Tian, H. Liang, *et al.*, "Reconfigurable, graphene-coated, chalcogenide nanowires with a sub-10-nm enantioselective sorting capability," *Microsyst. Nanoeng.* **4**(1), 7 (2018).
45. H. Zhang, L. Zhou, B. M. A. Rahman, *et al.*, "Ultra-compact Si-GST hybrid waveguides for nonvolatile light wave manipulation," *IEEE Photonics J.* **10**(1), 1–10 (2018).
46. R. Rajasekar, J. K. Jayabarathan, and S. Robinson, "Nano-optical filter based on multicavity coupled photonic crystal ring resonator," *Phys. E* **114**, 113591 (2019).
47. A. Tavousi and H. Heidarzadeh, "Realization of a multichannel drop filter using an ISO-centric all-circular photonic crystal ring resonator," *Photonics Nanostructures-Fundamentals Appl.* **31**, 52–59 (2018).
48. L. H. K. Duong, P. Yang, Z. Wang, *et al.*, "Crosstalk noise reduction through adaptive power control in inter/intra-chip optical networks," *IEEE Trans. Comput. Des. Integr. Circuits Syst.* **38**(1), 43–56 (2019).
49. U. Biswas, J. K. Rakshit, J. Das, *et al.*, "Design of an ultra-compact and highly-sensitive temperature sensor using photonic crystal based single micro-ring resonator and cascaded micro-ring resonator," *Silicon* **13**(3), 885–892 (2021).
50. G. Mohammadi, A. A. Orouji, and M. Danaie, "A high-performance and high-resolution optical refractive index sensor using a compact photonic crystal ring resonator," *Sens. Imaging* **25**(1), 26 (2024).
51. A. H. A. Nohoji and M. Danaie, "Highly sensitive refractive index sensor based on photonic crystal ring resonators nested in a Mach–Zehnder interferometer," *Opt. Quantum Electron.* **54**(9), 574 (2022).
52. M. Madhumitha and S. Selvendran, "Photonic crystal based narrowband optical filter: a brief analysis," *Optik* **228**, 166162 (2021).
53. A. Geravand, M. Danaie, and S. Mohammadi, "All-optical photonic crystal memory cells based on cavities with a dual-argument hysteresis feature," *Opt. Commun.* **430**, 323–335 (2019).
54. M. Mandal, P. De, S. Lakshan, *et al.*, "A review of electro-optic, semiconductor optical amplifier and photonic crystal-based optical switches for application in quantum computing," *J. Opt.* **52**(2), 603–611 (2023).
55. M. Danaie, R. N. Far, and A. Dideban, "Design of a high-bandwidth Y-shaped photonic crystal power splitter for TE modes," *Int. J. Opt. Photonics* **12**(1), 33–42 (2018).
56. M. Danaie and H. Kaatuzian, "Design of a photonic crystal differential phase comparator for a Mach–Zehnder switch," *J. Opt.* **13**(1), 015504 (2011).
57. R. Xu, P. Lv, F. Xu, *et al.*, "A survey of approaches for implementing optical neural networks," *Opt. & Laser Technol.* **136**, 106787 (2021).
58. G. Mohammadi, A. A. Orouji, and M. Danaie, "A tunable narrow single-mode bandpass filter using graphene nanoribbons for THz applications," *Sci. Rep.* **14**(1), 21217 (2024).
59. C. Sun, Y. Yu, and X. Zhang, "Ultra-compact waveguide crossing for a mode-division multiplexing optical network," *Opt. Lett.* **42**(23), 4913–4916 (2017).
60. L. Lu, M. Zhang, F. Zhou, *et al.*, "Inverse-designed ultra-compact star-crossings based on PhC-like subwavelength structures for optical intercross connect," *Opt. Express* **25**(15), 18355–18364 (2017).
61. J. Chen and Y. Shi, "Polarization-insensitive silicon waveguide crossing based on multimode interference couplers," *Opt. Lett.* **43**(24), 5961–5964 (2018).
62. W. Chang, L. Lu, X. Ren, *et al.*, "Ultra-compact dual-mode waveguide crossing based on subwavelength multimode-interference couplers," *Photonics Res.* **6**(7), 660–665 (2018).
63. M. M. Gilarue and S. H. Badri, "Photonic crystal waveguide crossing based on transformation optics," *Opt. Commun.* **450**, 308–315 (2019).
64. Z. Yu, A. Feng, X. Xi, *et al.*, "Inverse-designed low-loss and wideband polarization-insensitive silicon waveguide crossing," *Opt. Lett.* **44**(1), 77–80 (2019).
65. A. Geravand, M. Danaie, and E. Danaee, "Low cross-talk waveguide intersections for TE polarization using photonic crystals," *Opt. Commun.* **458**, 124838 (2020).
66. S. Chandran, M. Dahlem, Y. Bian, *et al.*, "Beam shaping for ultra-compact waveguide crossings on monolithic silicon photonics platform," *Opt. Lett.* **45**(22), 6230–6233 (2020).
67. Z. Dong, J. Qiu, Y. Chen, *et al.*, "Ultra-compact X-shaped waveguide crossings with flexible angles based on inverse design," *Opt. Express* **29**(13), 19715–19726 (2021).
68. X. Yuan, Y. Yang, X. Yan, *et al.*, "Ultra-compact multichannel optical waveguide crossings designed by a particle swarm optimized method," *Opt. Commun.* **503**, 127458 (2022).
69. B. Ni, C. Luo, H. Chen, *et al.*, "Compact and broadband dual-polarization waveguide crossing utilizing subwavelength-hole-assisted MMI couplers," *Opt. Lett.* **48**(22), 6040–6043 (2023).
70. J. Zhang, L. Xu, D. Mao, *et al.*, "Temperature-insensitive and low-loss single-mode silicon waveguide crossing covering all optical communication bands enabled by curved anisotropic metamaterial," *Nanophotonics* **12**(21), 4095–4107 (2023).
71. E. Morales-Sánchez, E. F. Prokhorov, A. Mendoza-Galván, *et al.*, "Determination of the glass transition and nucleation temperatures in Ge 2 Sb 2 Te 5 sputtered films," *J. Appl. Phys.* **91**(2), 697–702 (2002).



72. A. Bouaza, A. Ibanez, J. Olivier-Fourcade, *et al.*, “Synthèse et caractérisation des chalcogénures vitreux d’antimoine, d’arsenic et de thallium,” *Mater. Res. Bull.* **22**(7), 973–984 (1987).
73. A. Sebastian, M. L. Gallo, and D. Krebs, “Crystal growth within a phase change memory cell,” *Nat. Commun.* **5**(1), 4314 (2014).
74. A. Rashidi, A. Hatef, and S. R. Entezar, “Thermally induced tuning of absorption in a  $\text{Ge}_2\text{Sb}_2\text{Te}_5$ -based one-dimensional Fibonacci quasicrystal,” *Opt. & Laser Technol.* **137**, 106831 (2021).
75. N. M. Tolkach, N. V. Vishnyakov, P. I. Lazarenko, *et al.*, “Optical switching in multilayer structures based on  $\text{Ge}_2\text{Sb}_2\text{Te}_5$ ,” in *Journal of Physics: Conference Series* (2020), Vol. 1695, p. 12075.
76. M. S. Nisar, X. Yang, L. Lu, *et al.*, “On-chip integrated photonic devices based on phase change materials,” *Photonics* **8**(6), 205 (2021).
77. S. Abdollahramezani, O. Hemmatyar, H. Taghinejad, *et al.*, “Tunable nanophotonics enabled by chalcogenide phase-change materials,” *Nanophotonics* **9**(5), 1189–1241 (2020).
78. N. V. Voshchinnikov, G. Videen, and T. Henning, “Effective medium theories for irregular fluffy structures: aggregation of small particles,” *Appl. Opt.* **46**(19), 4065–4072 (2007).
79. S. Rashidi, A. Rashidi, and S. R. Entezar, “Tunable NIR absorption in a  $\text{Ge}_2\text{Sb}_2\text{Te}_5$ -based 1D asymmetric nonlinear hybrid nanostructure,” *Opt. & Laser Technol.* **157**, 108664 (2023).
80. T. G. Mayerhöfer, S. Pahlow, and J. Popp, “The Bouguer-Beer-Lambert law: shining light on the obscure,” *ChemPhysChem* **21**(18), 2029–2046 (2020).
81. N. Zobeiry and K. D. Humfeld, “A physics-informed machine learning approach for solving heat transfer equation in advanced manufacturing and engineering applications,” *Eng. Appl. Artif. Intell.* **101**, 104232 (2021).
82. M. Vajdi, F. S. Moghanlou, F. Sharifianjazi, *et al.*, “A review on the Comsol Multiphysics studies of heat transfer in advanced ceramics,” *J. Compos. Compd.* **2**(1), 35–44 (2019).
83. A. V. Kiselev, V. V. Ionin, A. A. Burtsev, *et al.*, “Dynamics of reversible optical properties switching of  $\text{Ge}_2\text{Sb}_2\text{Te}_5$  thin films at laser-induced phase transitions,” *Opt. Laser Technol.* **147**, 107701 (2022).
84. T. Kunkel, Y. Vorobyov, M. Smayev, *et al.*, “Crystallization of GST225 thin film induced by a single femtosecond laser pulse: Experimental and theoretical study,” *Mater. Sci. Semicond. Process.* **139**, 106350 (2022).
85. D. Z. Hu, R. S. Xue, and J. S. Zhu, “Study of crystallization in  $\text{Ge}_2\text{Sb}_2\text{Te}_5$ ,” *Integr. Ferroelectr.* **96**(1), 153–159 (2008).
86. K. Shirzad and C. Viney, “A critical review on applications of the Avrami equation beyond materials science,” *J. R. Soc. Interface* **20**(203), 20230242 (2023).
87. Y. Wang, L. Yin, W. Huang, *et al.*, “Optoelectronic synaptic devices for neuromorphic computing,” *Adv. Intell. Syst.* **3**(1), 2000099 (2021).
88. H. K. Li, T. P. Chen, P. Liu, *et al.*, “A light-stimulated synaptic transistor with synaptic plasticity and memory functions based on  $\text{InGaZnO}_x\text{-Al}_2\text{O}_3$  thin film structure,” *J. Appl. Phys.* **119**(24), 244505 (2016).
89. M. Lee, W. Lee, S. Choi, *et al.*, “Brain-inspired photonic neuromorphic devices using photodynamic amorphous oxide semiconductors and their persistent photoconductivity,” *Adv. Mater.* **29**(28), 1700951 (2017).
90. S. Qin, F. Wang, Y. Liu, *et al.*, “A light-stimulated synaptic device based on graphene hybrid phototransistor,” *2D Mater.* **4**(3), 035022 (2017).
91. H. Tan, Z. Ni, W. Peng, *et al.*, “Broadband optoelectronic synaptic devices based on silicon nanocrystals for neuromorphic computing,” *Nano Energy* **52**, 422–430 (2018).
92. Y. Yang, Y. He, S. Nie, *et al.*, “Light stimulated IGZO-based electric-double-layer transistors for photoelectric neuromorphic devices,” *IEEE Electron Device Lett.* **39**(6), 897–900 (2018).
93. Y. Liu, W. Huang, X. Wang, *et al.*, “A hybrid phototransistor neuromorphic synapse,” *IEEE J. Electron Devices Soc.* **7**, 13–17 (2019).
94. W. Alquraishi, Y. Fu, W. Qiu, *et al.*, “Hybrid optoelectronic synaptic functionality realized with ion gel-modulated  $\text{In}_2\text{O}_3$  phototransistors,” *Org. Electron.* **71**, 72–78 (2019).
95. Y. Zhang, J. B. Chou, J. Li, *et al.*, “Broadband transparent optical phase change materials for high-performance nonvolatile photonics,” *Nat. Commun.* **10**(1), 4279 (2019).
96. Z. Y. Ren, L. Q. Zhu, F. Yu, *et al.*, “Synaptic metaplasticity of protonic/electronic coupled oxide neuromorphic transistor,” *Org. Electron.* **74**, 304–308 (2019).
97. T. Li, Y. Wang, W. Li, *et al.*, “Structural phase transitions between layered indium selenide for integrated photonic memory,” *Adv. Mater.* **34**(26), 2108261 (2022).
98. F. Brücknerhoff-Plückelmann, I. Bente, M. Becker, *et al.*, “Event-driven adaptive optical neural network,” *Sci. Adv.* **9**(42), eadi9127 (2023).